scientific reports

OPEN

LOX$^+$ iCAFs in HNSCC have the potential to predict prognosis and immunotherapy responses revealed by single cell RNA sequencing analysis

Xue Liu[1,4,6], Huibing Li[2,4,6], Yanjin Wang[2,4], Qian Zhang[5], Yuehua Liu[3,4]✉ & Tingjiao Liu[2,4]✉

Carcinoma-associated fibroblasts (CAFs) exhibit significant heterogeneity and are closely associated with progression, resistance to anticancer therapies, and poor prognosis in head and neck squamous cell carcinoma (HNSCC). However, the specific functional role of CAFs in HNSCC has been inadequately explored. In this study, we utilized a single-cell RNA sequencing dataset from HNSCC (GSE103322) to recluster CAFs via the Seurat pipeline. On the basis of the reported markers, we identified two CAF subtypes, LOX-myCAFs and LOX + iCAFs, and generated signature markers for each. Through unsupervised consensus clustering, we identified and characterized two molecular subtypes of HNSCC-TCGA, each exhibiting distinct dysregulated cancer hallmarks, immunological tumor microenvironments, and stemness characteristics. The robustness of the LOX + iCAF-related signature clustering, particularly in terms of prognosis and prediction of immunotherapeutic response, was validated in an ANOVA cohort via a GEO dataset (GSE159067) consisting of 102 HNSCC patients. A positive correlation was validated between the expression of LOX and that of CD86, a marker of M1 macrophage polarization. Further experiments involving the coculture of conditioned medium derived from LOX-silenced CAFs with CAL-27 and UM-SCC-1 cell lines revealed that LOX silencing led to decreased proliferation and migration of these cancer cells, which was mediated by epithelial-mesenchymal transition (EMT) through IL-34- induced CSF1R/Akt signaling. In summary, our single-cell and bulk RNA sequencing analyses revealed a LOX + iCAF-related signature that can predict the prognosis and response to immunotherapy in HNSCC patients. Additionally, the LOX gene was identified as a promising therapeutic target for HNSCC treatment.

Keywords Head and neck squamous cell carcinoma, LOX, Inflammatory carcinoma-associated fibroblast, Prognostic signature, Immunotherapeutic response

Abbreviations

α-SMA	Alpha smooth muscle actin
ANOVA	Analysis of variance
CAFs	Carcinoma-associated fibroblasts
CM	Conditioned medium
CCK8	Cell Counting kit-8
DEGs	Differentially expressed genes

[1]Department of Multidisciplinary Consultant Center, Shanghai Key Laboratory of Craniomaxillofacial Development and Diseases, School of Stomatology, Shanghai Stomatological Hospital, Fudan University, Shanghai 200001, China. [2]Department of Oral Pathology, School of Stomatology, Shanghai Stomatological Hospital, Fudan University, Tianjin Road No.2, Huangpu District, Shanghai 200001, China. [3]Department of Orthodontics, Shanghai Stomatological Hospital & School of Stomatology, Fudan University, East Beijing Road No.356, Huangpu District, Shanghai 200001, China. [4]Shanghai Key Laboratory of Craniomaxillofacial Development and Diseases, Fudan University, Tianjin Road No.2, Huangpu District, Shanghai 200001, China. [5]Department of Oral Pathology, Dalian Stomatological Hospital, Changjiang Road No.935, Shahekou District, Dalian 116021, China. [6]Xue Liu and Huibing Li contributed equally to this work. ✉email: liuyuehua@fudan.edu.cn; tingjiao_liu@fudan.edu.cn

ECM	Extracellular matrix
EMT	Epithelial-mesenchymal transition
ECL	Enhanced chemiluminescence
FBS	Fetal bovine serum
FAP	Fibroblast activation protein
GSEA	Gene set enrichment analysis
GO	Gene ontology
HNSCC	Head and neck squamous cell carcinoma
H&E	Hematoxylin and eosin
iCAFs	Inflammatory CAFs
KEGG	Kyoto encycolpedia of genes and genomes
LOX	Lysyl oxidase
myCAFs	Myofibroblastic CAFs
NFs	Normal fibroblasts
OSCC	Oral squamous cell carcinoma
PMA	Phorbol 12-myristate 13-acetate
PCA	Principal component analysis
scRNA-seq	Single-cell RNA sequencing
SDS-PAGE	Sodium dodecyl sulfate-polyacrylamide gel
t-SNE	T-distributed stochastic neighbor embedding
TCGA	The Cancer Genome Atlas
TEX	T-cells exhaustion
TME	Tumor microenvironment
TPM	Transcripts per million

Carcinoma-associated fibroblasts (CAFs) are the most abundant cellular component in the tumor microenvironment (TME) and play a pivotal role in tumor progression[1]. CAFs not only interact directly with cancer cells, but also influence other components of the TME[2]. They secrete a variety of cytokines, extracellular vesicles, and other substances that contribute to the remodeling of the extracellular matrix (ECM)[3,4]. The origin, phenotype, and functions of CAFs are highly diverse, reflecting their significant heterogeneity within the TME[5].

Lysyl oxidase (LOX) is highly expressed in the stroma of oral squamous cell carcinoma (OSCC)-derived CAFs, where it catalyzes the cross-linking of collagen, leading to increased matrix stiffness[6]. Extracellular vesicle-rich LOX derived from CAFs promotes the crosslinking of collagen I, which drives the epithelial-mesenchymal transition (EMT) of OSCC via the FAK/paxillin/YAP signaling pathway[7]. A novel nanosystem has been developed to target the TME by utilizing LOX to catalyze the oxidation of lactic acid, while simultaneously releasing glycolysis inhibitors to eliminate the source of lactic acid and achieve antitumor metabolic therapy by blocking the ATP supply[8]. The "carrier-free" nanomedicine LOX@MnS converts lactic acid into cytotoxic ROS through a cascade reaction and further induces metabolic inhibition, enhancing the therapeutic effect and effectively activating the immune system to suppress tumors[9]. These strategies highlight the potential of LOX in immunotherapy, particularly in regulating the TME and demonstrating synergistic effects when combined with other therapeutic methods.

With the increasing attention given to CAFs and advancements in single-cell RNA sequencing (scRNA-seq) technology, researchers have increasingly investigated the heterogeneity of CAFs in various cancers[10]. Among these, two key subtypes have been identified: myofibroblastic CAFs (myCAFs) and inflammatory CAFs (iCAFs)[11]. myCAFs are characterized by high expression of alpha smooth muscle actin (α-SMA) and are recognized as significant contributors to the production and remodeling of the ECM[11]. These myCAFs play crucial roles in activating NF-κB signaling pathways in cancer cells, thereby promoting tumor cell proliferation and contributing to their resistance to chemotherapy[12]. On the other hand, iCAFs, which express low levels of α-SMA, are known for their ability to secrete high levels of inflammatory cytokines, such as IL-1 and IL-6[11]. These cytokines can promote tumor growth and mediate immunosuppression[13]. Research has shown that iCAFs can induce antigen-specific deletion of $CD8^+$ T cells, effectively shielding tumor cells from immune attack[14]. Moreover, iCAFs have been found to interact with other components of the TME, including endothelial cells and myeloid cells, suggesting their potential role in modulating the TME to support cancer progression[15]. In terms of therapeutic applications, targeting iCAFs or their secreted factors represents a promising strategy to increase the efficacy of immunotherapy. For example, inhibiting the functions of iCAFs, which are responsible for the induction of immune suppressor cell types, has been explored as a potential treatment approach[16]. By disrupting these interactions, it may be possible to reduce the immunosuppressive environment within tumors and improve the overall effectiveness of cancer therapies.

In summary, we integrated head and neck squamous cell carcinoma (HNSCC) scRNA-seq data and a HNSCC-TCGA dataset and identified a subtype of CAFs, LOX + iCAFs. Subsequent analyses revealed that the LOX + iCAF-related signature affected patient prognosis and immunotherapy response. Moreover, conditioned medium (CM) derived from LOX-silenced CAFs reduced the M1 polarization of macrophages. Coculture of CM derived from LOX-silenced CAFs with CAL-27 and UM-SCC-1 cells revealed that LOX silencing led to decreased proliferation and migration of these cancer cells, thereby causing EMT in OSCC through the CSF1R/Akt signaling pathway. Moreover, we performed single-cell and bulk RNA sequencing analyses and identified a LOX + iCAF-related signature that can predict the prognosis and response to immunotherapy in HNSCC patients.

Results

scRNA-seq analysis highlights the importance of LOX + iCAFs in HNSCC

In the analysis of the HNSCC single-cell sequencing dataset (Fig. 1A), nine distinct clusters were annotated via Seurat clustering on the basis of specific markers[17,18]. Previous studies have demonstrated that LOX is highly expressed in CAFs derived from HNSCC[6,7]. Consequently, we further identified LOX-CAF and LOX + CAF-related subtypes on the basis of the LOX expression level within these clusters (Fig. 1B). The lists of genes associated with the LOX-CAF and LOX + CAF signatures are provided in Table S1. t-SNE visualization revealed that LOX, a key player in catalytic activities related to the assembly of the ECM, was exclusively expressed in LOX + CAFs (Fig. 1B). A heatmap analysis revealed that contractile proteins (PDGFA, MCAM, MYLK, MYH11, and ACTA2) were predominantly expressed in LOX-CAFs, whereas immune and inflammatory proteins (FBLN1, CXCL12, CXCL14, and CD74) were primarily expressed in LOX + CAFs (Fig. 1C). Vlnplots further demonstrated the expression levels of each marker in LOX-CAFs and LOX + CAFs (Fig. 1D, S1A and B). On the basis of these findings, we designated these clusters "LOX-myCAFs" and "LOX + iCAFs,", respectively. Enrichment analyses indicated that LOX-myCAFs were associated with the regulation of cell–cell adhesion, whereas the collagen-containing extracellular matrix and extracellular matrix structure organization were predominantly enriched in LOX + iCAFs (Fig. 2A, B). Moreover, gene set enrichment analysis (GSEA) demonstrated that markers of EMT were upregulated in LOX + iCAFs (Fig. 2C), whereas myogenesis markers were upregulated in LOX-myCAFs (Fig. 2D).

Survival analysis highlighted the prognostic significance of LOX-myCAFs and LOX + iCAFs in HNSCC (Fig. S1C). Additionally, the LOX + iCAF subtype was correlated with older age and advanced-stage disease (stage III) (Fig. S1D). Collectively, these findings suggest that LOX + iCAFs are associated with disease progression and an unfavorable prognosis in HNSCC patients. This study further explored the biological roles of LOX + iCAFs and their associated cell markers.

The LOX + iCAF-related signature shaped the inflamed and immunosuppressive TME of HNSCC

To further investigate the pivotal role of LOX + iCAFs in shaping the TME, we decoded the TME composition via several established methodologies. By analyzing 28 immune-related signatures, two distinct immunity subtypes were identified through unsupervised hierarchical clustering: high and low-immunity subtypes (Fig. 3A). The high-immunity subtype was characterized by high stromal, immune, and ESTIMATE scores coupled with low tumor purity (Fig. 3B). Additionally, this subtype exhibited high infiltration levels of macrophages, $CD4^+$ T cells, and $CD8^+$ T cells. Interestingly, M1 macrophages and Tregs also highly infiltrated the high- immunity subtype, highlighting the heterogeneity and complexity of the TME in HNSCC (Fig. 3C). GSEA revealed that the high-immunity subtype was associated with inflammatory responses, IL2/STAT5 signaling, and TNFA via NF-κB signaling (Fig. 3D, S2A). To elucidate the role of LOX + iCAFs in the TME of HNSCC, we analyzed the correlation between the LOX + iCAF-related signature score and HNSCC immune subtypes. The results demonstrated that the LOX + iCAF-related signature was significantly upregulated in the high-immune subtype (Fig. 3A, B). Notably, the LOX + iCAF-related scores decreased progressively from the high-immunity subtype to the low-immunity subtype (Fig. 3B). On the basis of these findings, we speculate that LOX + iCAFs contribute to an inflammatory TME with a pro-tumoral phenotype in HNSCC. Owing to the presence of complex immunosuppressive signaling networks, a substantial number of infiltrating $CD8^+$ T cells in this TME are classified as "exhausted"[19,20]. The exhausted T-cell subtype is characterized by increased and sustained expression of inhibitory receptors, leading to a loss of effector function. We further explored the relationship between exhausted T cells and the LOX + iCAF-related signature and revealed a strong positive correlation ($R = 0.37$, Fig. S2B). To validate these findings, we decoded the TME via three additional methodologies: quanTIseq, TIMER, and MCPcounter. These methods confirmed that $CD8^+$ T cells highly infiltrated the TME of HNSCC patients with high LOX + iCAF-related scores (Fig. S2C).

Our findings suggest that LOX + iCAFs play a dominant role in shaping a pro-tumoral inflamed and immunosuppressive TME in HNSCC.

LOX + iCAF-related signature divides HNSCC into molecular subtypes with distinct biological features and Immunogenomic patterns

Two molecular subtypes of HNSCC-TCGA were identified through unsupervised hierarchical clustering on the basis of the LOX + iCAF-related signature (Fig. 4A). Cluster 1 clearly differed from Cluster 2, characterized by significantly higher LOX + iCAF-related scores (Fig. 4B, C). As illustrated in Fig. 4D, Cluster 1 was predominantly associated with the high-immunity subgroup, whereas the low-immunity subgroup was more related to Cluster 2. Further analysis of the TME revealed that Cluster 1 tumors were characterized by high stromal, immune, and ESTIMATE scores, as well as low tumor purity (Fig. 4E). Previous studies have reported T-cell exhaustion heterogeneity across various cancers, identifying five subclusters of exhausted T cells with diverse functional properties[11]. A progenitor-differentiated subtype of exhausted T cells was characterized by a signature of six genes (BTK, IL7R, LTB, PRF1, SP140, WAS). We assessed the expression of these six subtype-specific markers within our molecular subtypes and found that Cluster 1 was correlated with high expression levels (Fig. 4F). Additionally, factors associated with M1 macrophage polarization were upregulated in Cluster 1 (Fig. 4G). Collectively, these findings suggest that Cluster 1 may represent an immunosuppressive TME in HNSCC, characterized by high LOX + iCAF-related activities, elevated immune infiltration, and markers of T-cell exhaustion.

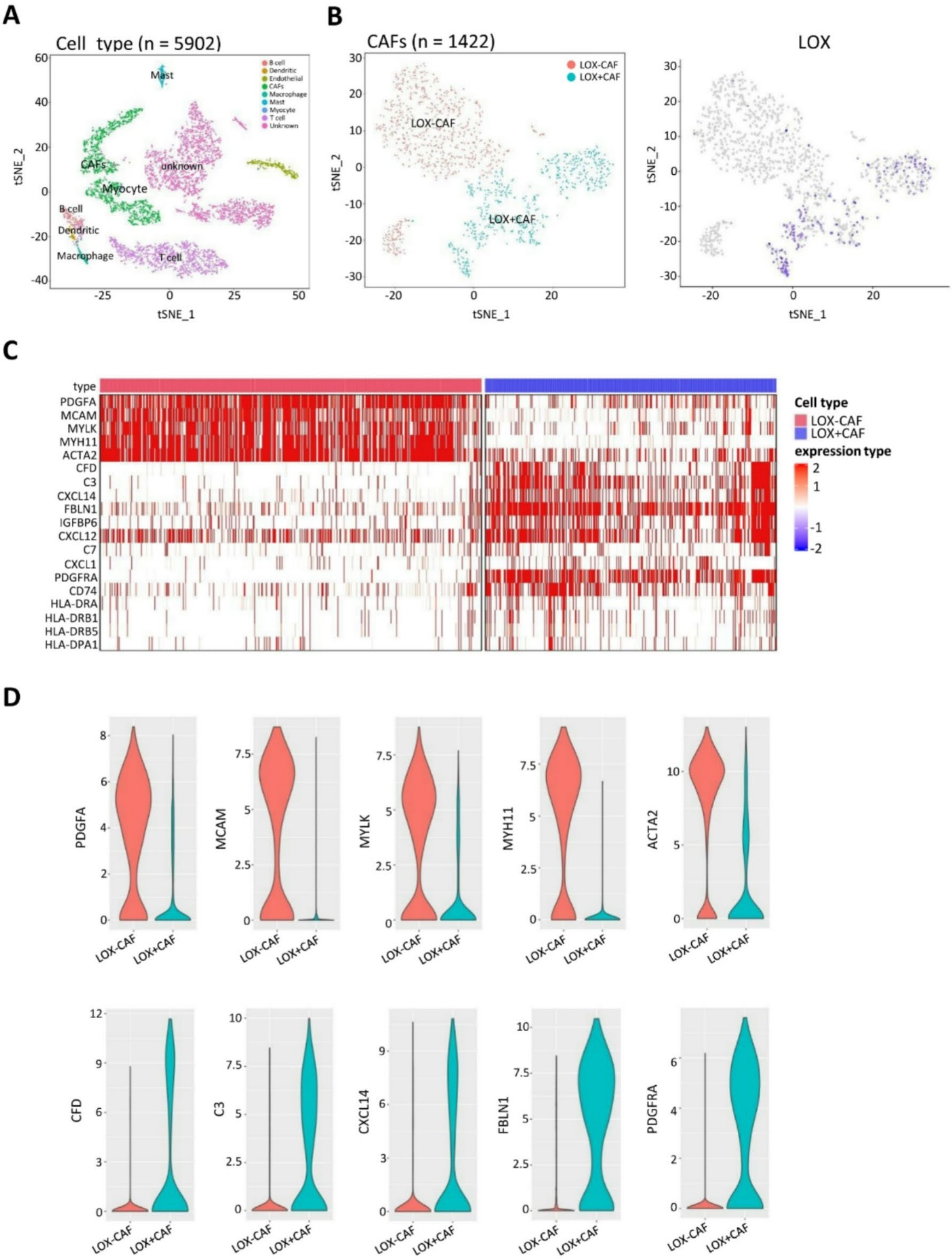

Fig. 1. Cell clustering and annotation of scRNA-seq. (A) Single-cell RNA sequencing dataset of HNSCC (GSE103322) were identified nine clusters previously based on reported markers, including B cell, Dendritic, Endothelial, CAFs, Macrophage, Mast, Myocyte, T cell, Unknown. (B) LOX-CAF and LOX + CAF were annotated by the LOX level of CAFs subtypes. t-SNE plots demonstrated the expression level of LOX in LOX-CAF and LOX + CAF. (C) The heatmap showed the expression differences in the top 9 cell-type specific markers between LOX-CAF and LOX + CAF. Colors ranging from blue to red presented from low to high. (D) Vnplots demonstrated the expression levels of each marker in LOX-CAF and LOX + CAF.

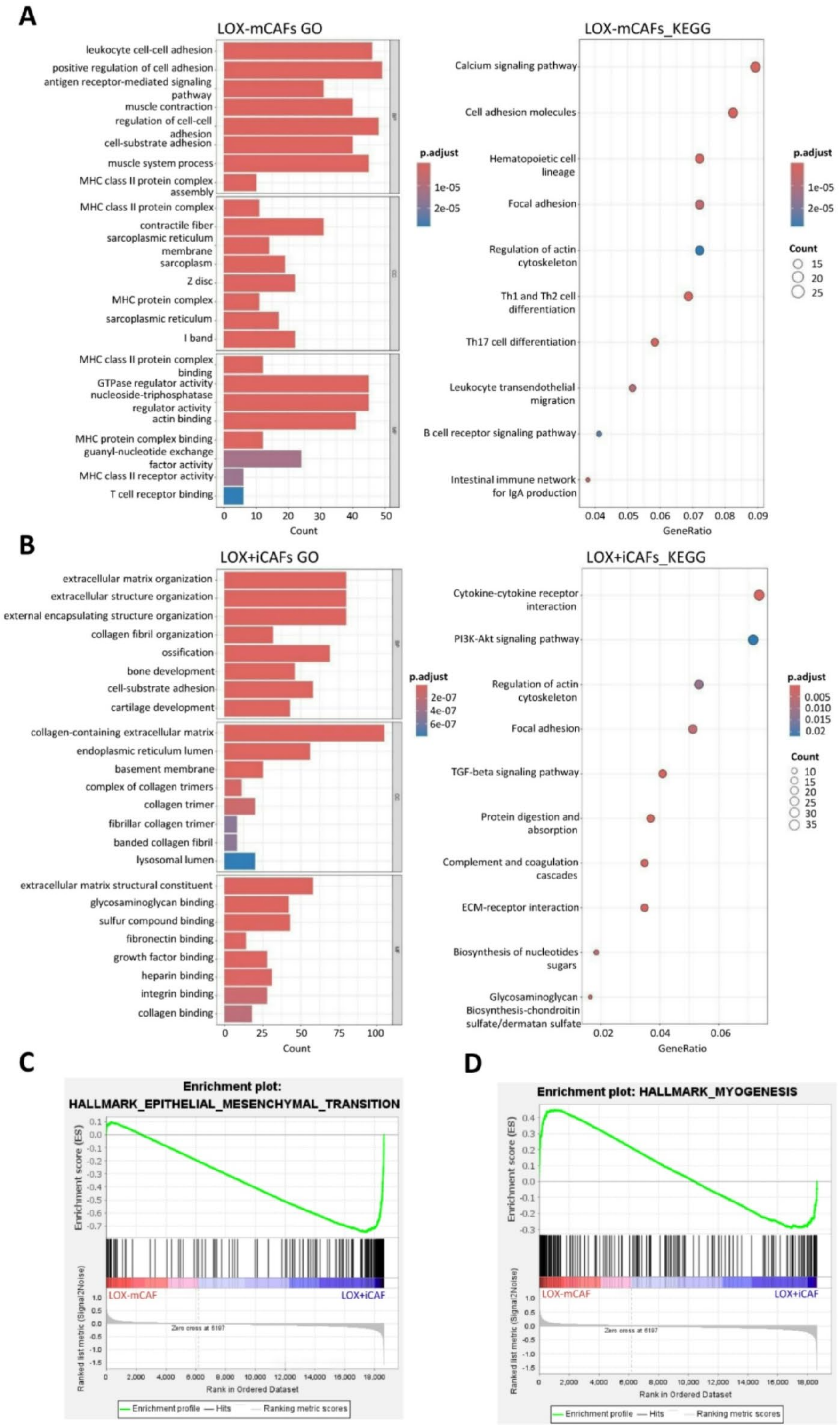

Fig. 2. GO and KEGG enrichment analysis of LOX-myCAFs and LOX + iCAFs subtypes. (A, B) LOX-myCAFs/LOX + iCAFs GO (Left) and KEGG (Right) analyzes demonstrated the enriched terms by specific markers of LOX-myCAFs (up) and LOX + iCAFs (bottom). (C, D) GSEA analysis revealed upregulated cancer hallmarks in LOX + iCAFs (Left) and LOX-myCAFs (Right), respectively.

LOX + iCAF-related subtypes had distinct dysregulated pathways

Compared with the patients in Cluster 2, those in Cluster 1 had a poorer prognosis (Fig. 5A) and a higher prevalence of basal/nonkeratinizing/NOS squamous cell carcinoma subtypes (Fig. 5B). In contrast, Cluster 2 had a greater proportion of keratinizing squamous cell carcinoma subtypes (Fig. 5B). Furthermore, the stemness-

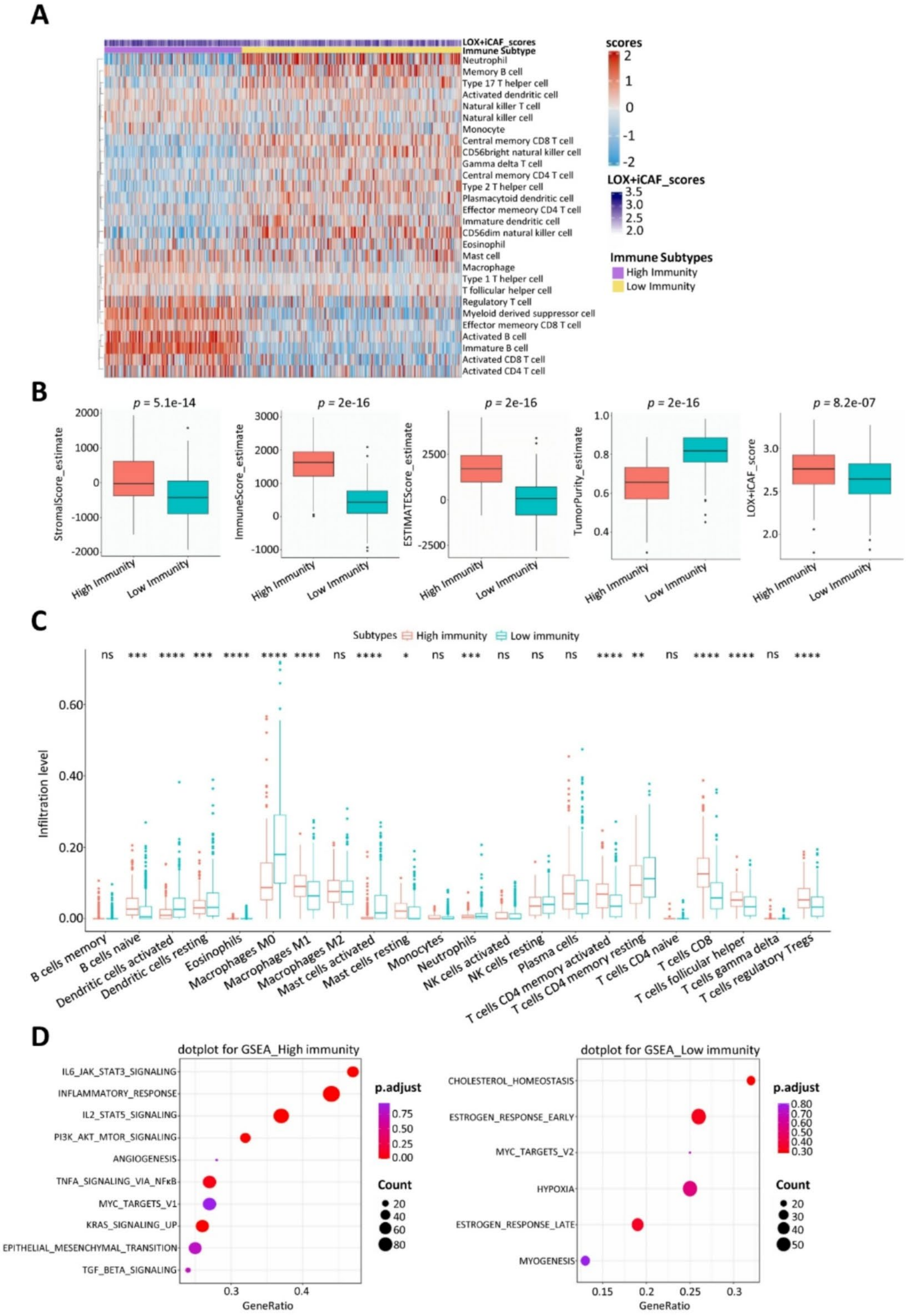

Fig. 3. LOX + iCAF-related signature guided an inflamed and immunosuppressive TME of HNSCC. (A) Two immunity subtypes were identified by unsupervised hierarchical clustering. (B) The distribution of stromal, immune, ESTIMATE score, tumor purity, and LOX + iCAF-related signature across two immunity subtypes. (C) The infiltration abundances of 22 immune cells across two immunity subtypes. (D) GSEA analysis revealed upregulated cancer hallmarks in two immunity subtypes.

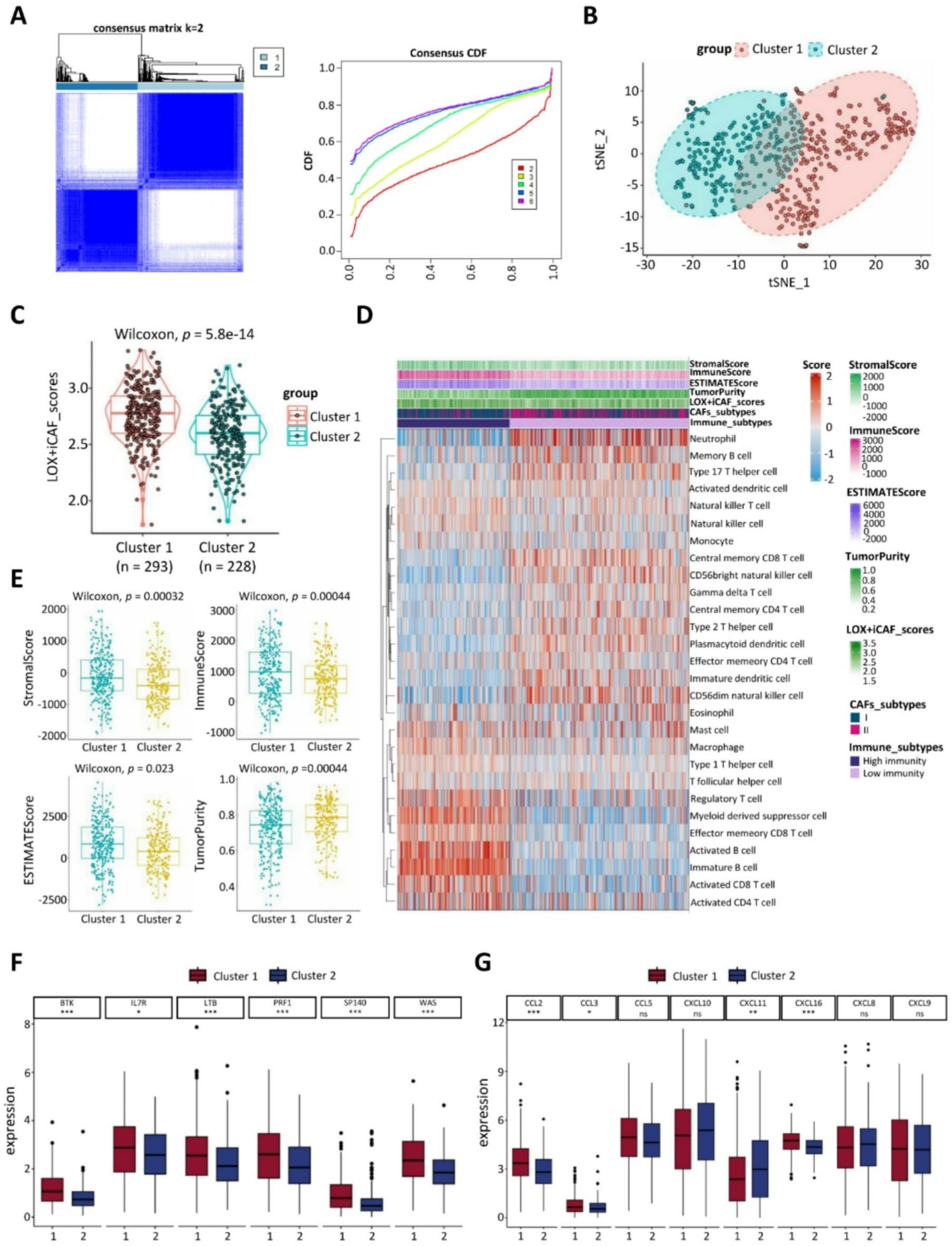

Fig. 4. LOX + iCAF-related signature is characterized with distinct biological features and immunogenomic patterns. (A) HNSCC-TCGA was identified into two molecular subtypes. (B) t-SNE plots showed the discrimination between the two subtypes. (C) Cluster 1 was featured with higher LOX + iCAF-related scores compared with Cluster 2. (D) The heatmap demonstrated two immunity subtypes with diverse stromal score, immune score, ESTIMATE score, tumor purity and LOX + iCAF-related scores. (E) The distribution of stromal score ($p = 0.00032$), immune score ($p = 0.00044$), ESTIMATE score ($p = 0.023$), tumor purity ($p = 0.00044$) between two molecular subtypes. The expression levels of progenitor-differentiated TEX signature genes (F) and M1 Macrophage polarization factors (G) between two subtypes. *ns*, not significance; $^{*}p < 0.05$; $^{**}p < 0.01$; $^{***}p < 0.001$.

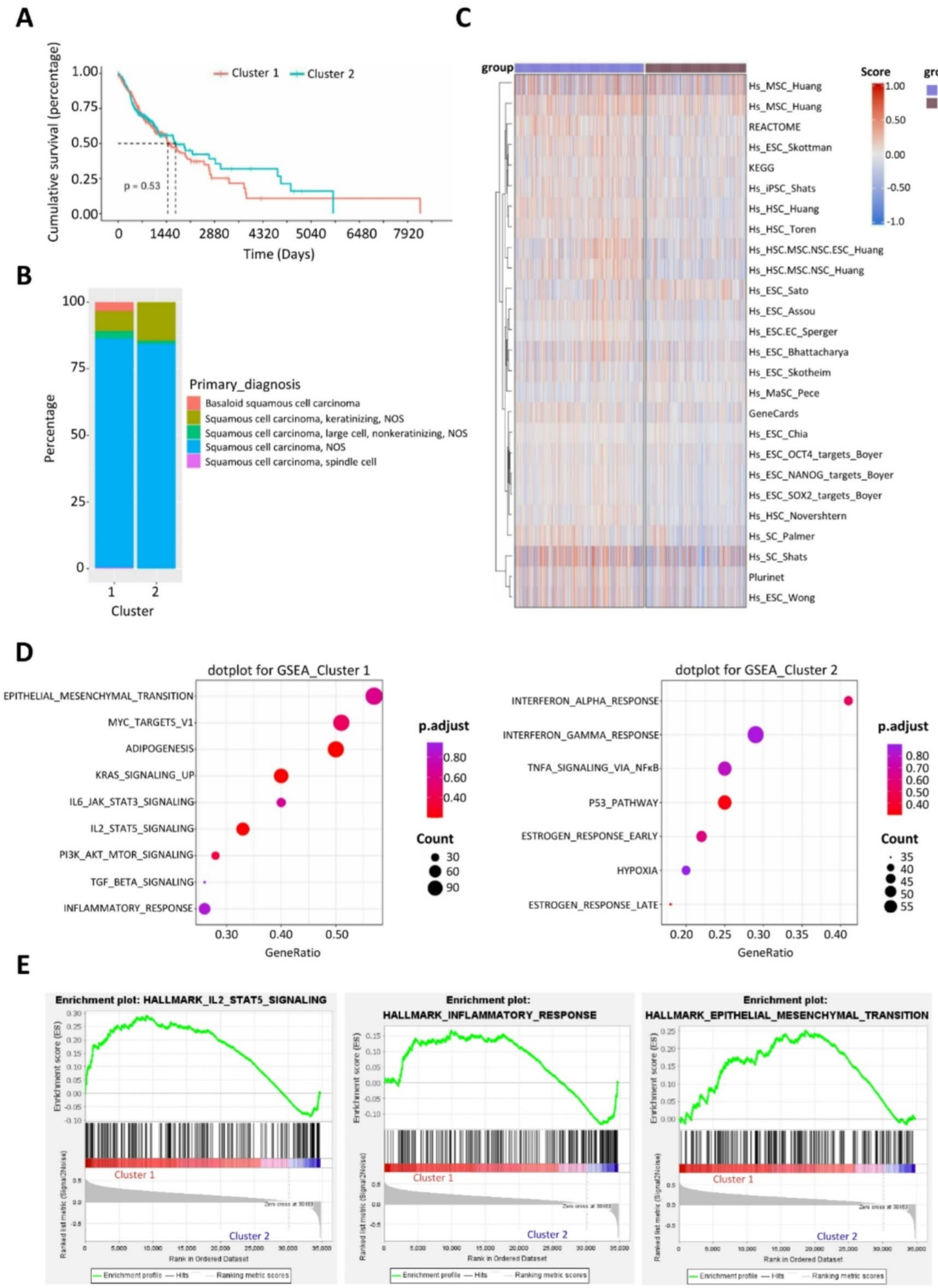

Fig. 5. LOX + iCAF-related subtypes had distinct dysregulated pathways. (A) Cluster 1 was related to a poorer prognosis in HNSCC-TCGA dataset. (B) Consensus TCGA molecular subtypes between two clusters. (C) The enrichment activity of 26 stemness-related signature between two clusters. (D) Upregulated cancer hallmarks of Cluster 1 (Left) and Cluster 2 (Right). (E) Upregulated pathways of Cluster 1 are presented.

related signature was predominantly upregulated in Cluster 1 (Fig. 5C). When the dysregulated hallmarks of cancer in these two molecular subtypes were investigated, GSEA revealed that Cluster 1 was significantly associated with EMT, the inflammatory response, and the IL2/STAT5 signaling pathway (Fig. 5D, E). These findings further support the notion that Cluster 1 is characterized by a more aggressive and immunosuppressive TME in HNSCC.

LOX + iCAF-related subtypes predict prognostic biomarkers of the response to PD-1/PD-L1 inhibitors in patients with HNSCC

The study compared the hot scores on the basis of the objective response to PD-1/PD-L1 inhibitor in the ANOVA cohort (Fig. 6A). The heatmap revealed that distinct expression profiles of CXCL1, CXCL14, IGFBP6, C3, CD74, PDGFRA, and CXCL12 were predominantly expressed in HOT tumors, which are more sensitive to PD-1/PD-L1 inhibitors. Conversely, PDGFA and ACTA2 were predominantly expressed in COLD tumors, which were less responsive to these inhibitors (Fig. 6B). The correlation coefficients of the hot score between the expression profiles of PDGFA, ACTA2, C3, CXCL14, IGFBP6, CXCL12, CXCL1, PDFGRA, and CD74 were analyzed (Fig. 6C). Correlation analysis revealed significant negative correlations between the hot score and the relative expression of PDGFA (Fig. 6D), whereas ACTA2 showed no significant negative correlation (Fig. 6D). On the other hand, there were significant positive correlations between the hot score and the relative expression of IGFBP6, C3, and CXCL12 (Fig. 6E). The distribution of CXCL14 in HOT tumors requires further investigation to clarify its correlation. These findings suggest that the LOX + iCAF-related signature is predominantly expressed in HOT tumors and may serve as a predictive biomarker for the response to PD-1/PD-L1 inhibitors in HNSCC patients. These findings indicate the potential for the use of LOX + iCAF-related signature to identify patients who are more likely to benefit from immunotherapy.

Clinical samples with the LOX + iCAF-related signature and modulated the proliferation and migration of OSCC

To explore the expression of the LOX + iCAF-related signature in HNSCC patients, the clinical parameters of four HNSCC tissue samples were collected (Table S2). Hematoxylin and eosin (H&E) staining confirmed the pathological features of HNSCC (Fig. 7A), and the coexpression of the LOX + iCAF-related signature proteins FBLN1 and CXCL12 was observed in the stromal regions of HNSCC tissue samples (Fig. 7B). Primary CAFs were isolated from two human OSCC samples, designated CAF-S5/-S6, whereas NFs were obtained from healthy human gingival tissues. The expression levels of pancytokeratin, vimentin, FAP, and α-SMA were assessed via immunofluorescence staining and western blotting (Fig. S3A, B). In these experiments, Pro-LOX (55 kDa) was highly expressed in CAF-S5/-S6 and slightly expressed in NFs, whereas it was barely detectable in UM-SCC-1 cells. Conversely, αLOX expression was extremely low in UM-SCC-1 cells, NFs, and CAF-S5/-S6 (Fig. 7C). To further investigate this phenomenon, CAF-S5/-S6 were transfected with si-NC, si-LOX-1136, or si-LOX-1277 to knockdown LOX expression. Both si-LOX-1136 and si-LOX-1277 effectively reduced LOX protein levels in the CAF-S5/-S6, which was consistent with a decrease in FBLN1 protein expression (Fig. 7D).

Given the role of LOX + iCAFs in guiding an immunosuppressive TME, the expression of the M1 polarization markers CD86 and iNOS was examined in macrophages treated with CM derived from CAF-S5/-S6 transfected with si-LOX-1136 and si-LOX-1277. The results demonstrated that LOX depletion significantly reduced the protein levels of CD86 and iNOS in macrophages (Fig. 7E). Additionally, CM from CAF-S5/-S6 transfected with si-NC increased the proliferation and migration abilities of CAL-27 and UM-SCC-1 cells, compared with CM from those transfected with si-LOX-1136 and si-LOX-1277 (Fig. 7F, G). These findings suggest that LOX knockdown in CAFs diminishes the proliferation and migration of OSCC cells, indicating a potential therapeutic target for modulating the TME in HNSCC.

IL34 promoted EMT in OSCC through the activation of CSF1R/Akt signaling

To further explore the mechanisms by which CM derived from LOX-silenced CAFs modulates OSCC cells, RNA sequencing was performed after LOX knockdown in CAF-S5/-S6. Principal component analysis (PCA) revealed a significant difference in gene expression patterns between the si-NC and si-LOX-1277 groups compared with the si-NC and si-LOX-1136 groups (Fig. 8A). A Venn diagram highlighted this distinction, revealing 306 genes shared between the groups and 1954 unique genes in the si-LOX-1277 vs. si-NC comparison (Fig. 8B). The heatmap further revealed significant downregulation of genes in both the si-NC and si-LOX-1136 groups and the si-NC and si-LOX-1277 groups (Fig. 8C). Volcano plots revealed 633 differentially expressed genes (DEGs), with 333 upregulated and 300 downregulated genes in the si-LOX-1277 vs. si-NC comparison (Fig. 8D). Among the top DEGs, IL34 was identified as the only soluble factor, known to promote tumor proliferation and activate the ERK signaling pathway in papillary thyroid cancer cells[21]. GSEA revealed that EMT was upregulated in the si-LOX-1277 vs. si-NC comparison (Fig. 8E). Gene Ontology (GO) annotation revealed that 20 biological processes were significantly affected, with notable changes in cell part, binding, and cellular processes in the si-LOX-1277 vs. si-NC comparison (Fig. 8F). Additionally, Kyoto Encycolpedia Of Genes and Genomes (KEGG) pathway analysis revealed significant enrichment of pathways such as MAPK and PI3K/Akt, which are closely associated with the EMT process in OSCC[22,23] (Fig. 8G). Further investigation revealed that the IL34 content in CM derived from CAF-S5/-S6 transfected with si-LOX-1277 was significantly greater than that in CM from CAF-S5/-S6 transfected with si-NC (Fig. 8H). Moreover, the expression level of pCSF1R (Tyr723) increased over time in CAL-27 and UM-SCC-1 cells treated with IL34 (100 ng/mL) at 0, 24, 48, and 72 h (Fig. 8I). To determine whether EMT in OSCC induced by IL34 activated the PI3K/Akt signaling pathway, experiments were performed, and the results revealed that treatment with MK-2206, a PI3K/Akt pathway inhibitor, along with IL34, significantly decreased the expression levels of pAkt (Ser473), N-cadherin, and vimentin in CAL-27 and UM-SCC-1 cells (Fig. 8J). Conversely, the same treatments increased the expression level of E-cadherin in these

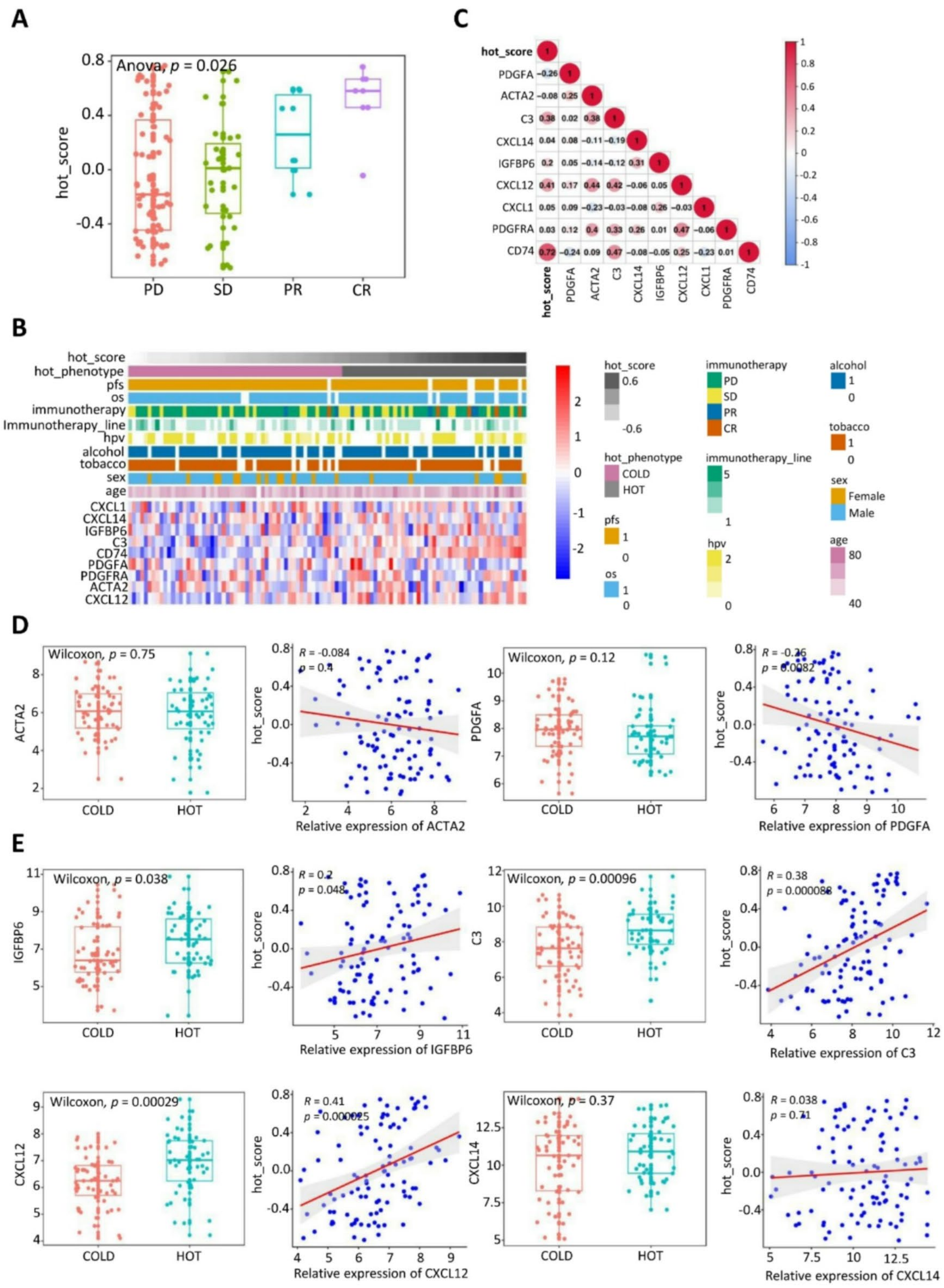

cells (Fig. 8J). These findings suggest that IL34 induces EMT in OSCC by activating the CSF1R/Akt signaling pathway, highlighting a potential therapeutic target for modulating tumor progression in HNSCC.

Discussion

CAFs, as major components of the TME, play multifaceted roles in tumor progression, including tumorigenesis, metastasis, immunomodulation, and drug resistance[3,24]. Given the remarkable heterogeneity of CAFs, identifying specific subtypes could provide promising therapeutic targets for HNSCC. However, the role of CAFs in the TME of HNSCC remains poorly.

understood. In this study, via the use of scRNA-seq data and the HNSCC-TCGA dataset, we identified the LOX + iCAF-related signature and stratified HNSCC into two molecular subtypes with diverse functional heterogeneities, including immune cell infiltration, dysregulated pathways, prognosis, and response to

◀**Fig. 6**. LOX + iCAF-related subtypes predicted prognostic biomarkers of response to PD-1/PD-L1 inhibitors in patients with HNSCC. (A) The Hot oral tumor (HOT) score was compared between patients according to the objective response in the Anova cohort (Kruskall Wallis Test) ($p = 0.026$). (B) The heatmap showed the expression of LOX + iCAFs signature in HNSCC patient with clinical parameters. (C) Correlation coefficients of hot score between LOX-myCAFs signature (ACTA2, PDGFA) and LOX + iCAFs signature (C3, CXCL14, IGFBP6, CXCL12, CXCL1, PDFGRA, CD74). (D) The distribution of ACTA2 ($p = 0.75$), PDGFA ($p = 0.12$) between two hot_phenotype types. Correlation coefficients between hot score and relative expression of ACTA2 (R = -0.084; $p = 0.2$), PDGFRA (R = -0.26; $p = 0.0082$). (E) The distribution of IGFBP6 ($p = 0.038$), C3 ($p = 0.00096$), CXCL12 ($p = 0.00029$), CXCL14 ($p = 0.37$) in two hot_phenotype types. Correlation coefficients between hot score and relative expression of IGFBP6 ($R = 0.2$; $p = 0.048$), C3 ($R = 0.38$; $p = 0.000088$), CXCL12 ($R = 0.41$; $p = 0.000025$), CXCL14 ($R = 0.038$; $p = 0.71$). PD: Progressive disease. SD: Stable disease. PR: Partial response. CR: Complete response.

immunotherapy. While single-cell sequencing in conjunction with TCGA offers insights into cellular diversity, it also encounters hurdles in data analysis and faces technical constraints. For instance, the sequencing depth is often restricted, potentially resulting in incomplete foundational datasets. The expense associated with this technology is considerable, which can impede its use in extensive research endeavors. Unlike traditional genomic sequencing methods, single-cell sequencing demands detailed sequencing, isolation, and quality assessment for each individual cell, which is resource-intensive in terms of labor, materials, and finances. In certain research scenarios, sample sizes might be constrained by the requirement for consistent treatment protocols and pharmaceutical types, which can impact the broader applicability and relevance of the findings. Despite the potential for integrating single-cell data with other omics datasets, there are ongoing challenges with the development and utilization of comprehensive multi-omics analysis tools, which can limit the thorough exploration and practical use of single-cell sequencing data.

LOX as a therapeutic target demands significant financial and resource allocation, encompassing stages from drug development to clinical trials and patient care. Crafting LOX-targeted medications hinges on comprehending its tumorigenesis mechanisms and devising strategies for secure and potent intervention. Additionally, the design and execution of clinical trials are complex and time-consuming. Varied patient responses to LOX therapy underscore the need for accurate biomarker analysis to forecast treatment success and identify suitable candidates. New drug development mandates thorough evaluation of side effects and safety to ensure patient compliance and sustained treatment. The potential for tumor resistance to LOX therapy mandates continuous research for overcoming or managing such resistance issues. LOX-targeted therapy may need to be used in combination with other therapeutic approaches (such as chemotherapy and radiotherapy, etc.) to improve treatment outcomes. This requires the development of comprehensive treatment strategies and the assessment of synergistic effects of different treatment methods.

Our results demonstrated that CM derived from LOX-silenced CAFs decreased M1 macrophage polarization and tumor progression. CAFs are known to secrete various growth factors, kinases, cytokines, and chemokines into the TME, facilitating tumor progression[25]. High expression of LOX has been reported in the stroma of several malignant tumors and is associated with processes such as ECM remodeling and metastasis[26,27]. In our study, LOX was highly expressed in CAFs but only slightly expressed in NFs (Fig. 7C). Further investigation into the mechanisms of LOX in the TME of HNSCC revealed two distinct subtypes, LOX-myCAFs and LOX + iCAFs, identified by reclustering CAFs via Seurat. The LOX + iCAF-related signature was associated with various dysregulated pathways, including those related to ECM organization, cytokine-cytokine receptor interactions, focal adhesion, TGF-β signaling, and EMT. Notably, HNSCC tumors with an upregulated LOX + iCAF-related signature presented an inflamed TME, poor prognosis, high infiltration of M1 macrophages, and dysregulated cancer hallmarks. Despite the inflamed TME typically being associated with antitumor functions and favorable prognosis, our findings suggest that LOX + iCAFs may induce a protumoral inflamed TME, potentially through the secretion of proinflammatory cytokines and factors[28]. CD8$^+$ T cells, often associated with antitumor immunity, appeared to be exhausted in the presence of LOX + iCAFs, characterized by elevated inhibitory marker levels and poor effector function.

Unsupervised clustering identified two distinct molecular subtypes in HNSCC-TCGA. Compared with Cluster 2, Cluster 1 presented higher LOX + iCAF-related scores, indicating a poor prognosis, and upregulation of the stemness-related signature. Enrichment analysis revealed that Cluster 1, with an upregulated signature was related to the IL-2/STAT5 signaling pathway, inflammatory responses, and EMT. In combination with their crosstalk with tumor cells, LOX + iCAFs are responsible for tumor initiation, progression, invasion, and metastasis[29]. In this study, a significant positive correlation was detected between the T-cell exhaustion (TEX)-associated signature and the LOX + iCAF-related signature. Furthermore, six progenitor-differentiated TEX subtype-specific genes, BTK, IL7R, LTB, PRF1, SP140 and WAS, were positively correlated with the LOX + iCAF-related signature. Moreover, three terminally-differentiated TEX subtype-specific genes, RBM10, AXIN2 and MS2, were negatively correlated with the LOX + iCAF-related signature (data not shown). Infiltrated M1 macrophages with upregulated M1 polarization factors. Moreover, Tregs were not highly expressed. The presence of these cells in the TME resulted in an immunosuppressive phenotype, and correspondingly, the response to PD-1/PD-L1 inhibitors was impaired in this cluster.

In combination with the results from the ANOVA cohort, the HOT scores of 102 patients with HNSCC treated with immunotherapy targeting PD-1/PD-L1 in the context of clinical trials (are shown in Fig. 6A). The signature associated with LOX-myCAFs, including ACTA2 and PDGFA, is predominantly found in COLD tumors. Moreover, there was a negative correlation between the expression of ACTA2 and PDGFA and the

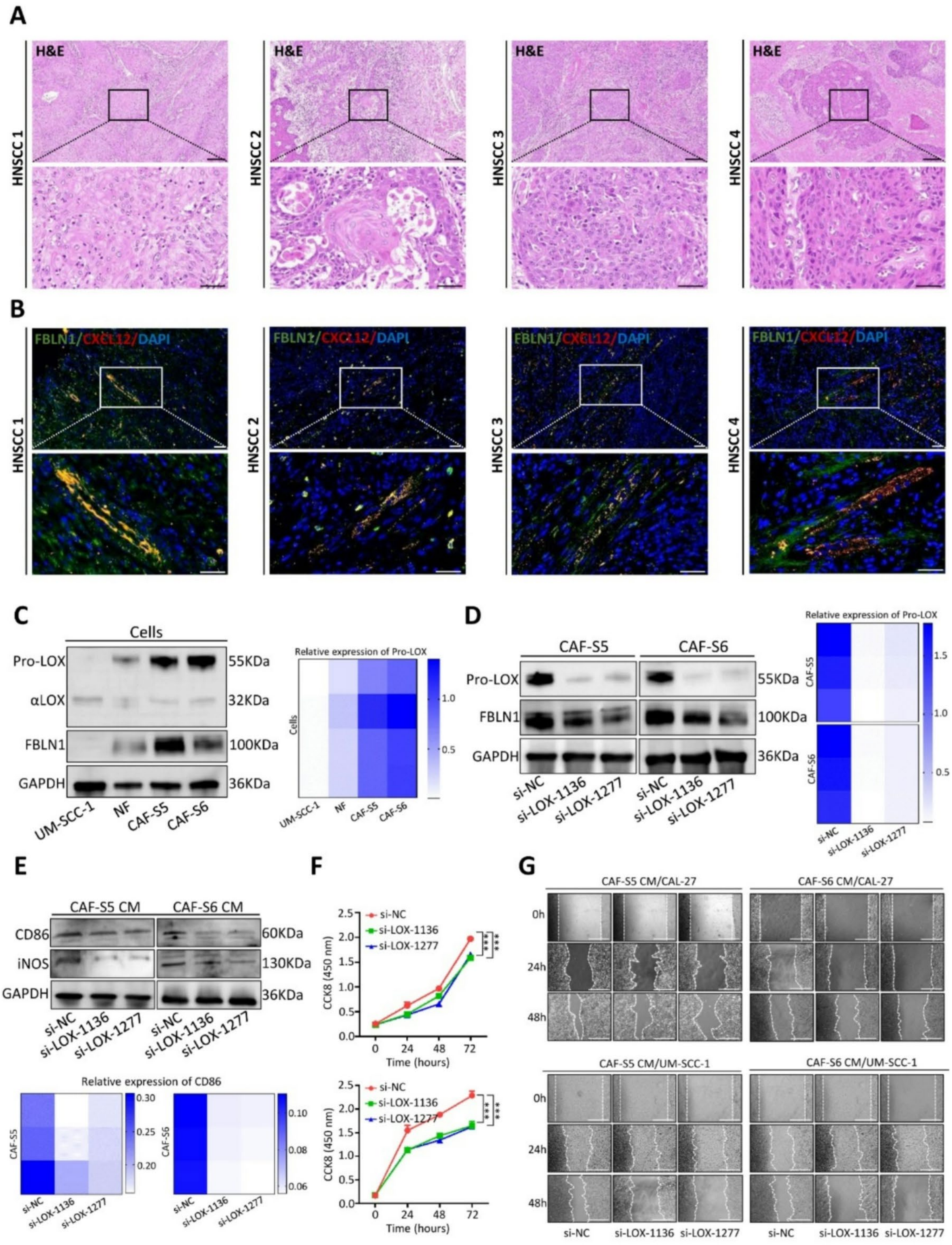

hot score. Interestingly, the LOX + iCAF-related signature, characterized by the presence of IGFBP6, C3, and CXCL2, is expressed mainly in HOT tumors. The signature related to LOX + iCAFs was positively correlated with the hot score, indicating a potential link between the expression of the LOX + iCAF-related signature and response to immunotherapies. However, the correlation between the expression of CXC14 and the hot score remains to be confirmed.

In vitro studies further supported these findings, showing that conditioned medium (CM) from LOX-silenced CAFs not only reduced the expression of CD86 and iNOS in macrophages but also decreased the proliferation and migration of OSCC cells through IL34 signaling. RNA sequencing analysis indicated that the CSF1R/Akt signaling pathway, which is activated by IL34, plays a critical role in promoting EMT in OSCC. Overall, this study underscores the potential of targeting LOX within CAFs as a therapeutic strategy to inhibit tumor progression and improve the prognosis and sensitive response to PD-1/PD-L1 inhibitors in HNSCC. Our

◀**Fig. 7**. Expression pattern of LOX + iCAF-related signature and regulated the proliferation and migration of OSCC. (A, B) H&E and the co-expression of CXCL12, FBLN1 in HNSCC-1/-2/-3/-4 tissues examined by immunofluorescence staining. Blue indicating DAPI. Scale bar = 100 µm, 50 µm, 20 µm (C) The expression levels of Pro-LOX, FBLN1 in UM-SCC-1, NF and CAF-S5/-S6 examined by western blot (*n* = 3 per group). GAPDH used as internal control. Left: representative images. Right: quantification analysis of Pro-LOX in different groups. (D) The expression levels of Pro-LOX, FBLN1 in CAF-S5/-S6 induced by transfection with si-LOX-1136 and si-LOX-1277 compared with si-NC (*n* = 3 per group). Left: representative images. Right: quantification analysis of Pro-LOX in different groups. (E) Macrophages treated by CM-derived from CAF-S5/-S6 induced by transfection with si-NC, si-LOX-1136 and si-LOX-1277 and the expression of CD86 and iNOS was subjected to western blot. Up: representative images. Bottom: quantification analysis of CD86 in different groups. (F) The proliferation of CAL-27 and UM-SCC-1 treated by CM of CAF-S5/-S6 induced by transfection with si-NC, si-LOX-1136 and si-LOX-1277 examined by CCK8 assay (*n* = 3 per group). (G) The migration abilities of CAL-27 and UM-SCC-1 treated by CM of CAF-S5/-S6 induced by transfection with si-NC, si-LOX-1136 and si-LOX-1277 examined by wound healing assay (*n* = 3 per group) Scale bar = 200 µm. For blots source data, see Fig. S4. *** *P* < 0.001.

findings suggest that inhibiting stromal LOX could significantly impact the TME, reduce tumor cell growth and migration, and improve immunotherapy efficacy in HNSCC.

Conclusion

Through integrated single-cell and TCGA datasets, we identified signatures of LOX-myCAFs and LOX + iCAFs, which categorized HNSCC patients into two subtypes characterized by unique molecular features. The signature associated with LOX + iCAFs demonstrated to be robust in predicted prognosis and immunotherapy response in the TCGA and GEO datasets. Subsequent analyses identified the LOX + iCAF-related signature that predicted poor prognosis, impaired immune reaction, and M1 infiltration. Furthermore, in vitro co-culture experiments verified that LOX-silenced CAFs regulated the M1 polarization, proliferation and migration capabilities of macrophages and OSCC cell lines, driven by EMT of OSCC through IL34 activated CSF1R/Akt signaling. LOX may emerge as a promising target for HNSCC treatment.

Materials and methods

Data acquisition and analysis

HNSCC single-cell RNA sequencing (scRNA-seq) dataset was obtained from the Gene Expression Omnibus (GEO, https://www.ncbi.nlm.nih.gov/geo/) under the accession number GSE103322[17]. This dataset included 5902 single cells from 18 HNSCC patient samples. The data analysis was conducted using R software, specifically utilizing the Seurat package[30]. Standard quality control measures were applied to the ensure data integrity, employing the following criteria of 200 < nFeature-RNA < 5000 and percent.mt < 20%, and highly variable genes were selected based on the top 2000 genes exhibiting the highest variance. Non-linear dimensional reduction was performed using the t-distributed stochastic neighbor embedding (t-SNE) method, applying 15 principal components and a resolution of 0.7. The CAFs were re-clustered into two subclusters, LOX-myCAFs and LOX + iCAFs, using the FindClusters function within Seurat. Transcriptome FPKM (fragments per kilobase of transcript per million fragments mapped) data for HNSCC patients were downloaded from The Cancer Genome Atlas (TCGA) database (https://portal.gdc.cancer.gov/). To address and remove batch effects within each subgroup, the Harmony software (version 0.1.0) was utilized. Subsequent re-analysis of cells within each group followed the standard Seurat protocol. A dataset with HNSCC patients treated with PD-1/PD-L1 inhibitors along with clinical parameters was downloaded. Additionally, 26 stemness-related gene sets were obtained from the StemChecker web tool (http://stemchecker.sysbiolab.eu/, accessed on November 12, 2022)[31]. The TEX-associate d signature and 28 immune-related signature was retrieved from the supplementary files of relevant studies[32,33].

Unsupervised clustering and biological properties examination

Using the LOX + iCAF-related signature, unsupervised clustering was conducted via the R package ConsensusClusterPlus[34]. To reduce the dimensionality of the scRNA-seq dataset, PCA was performed on the top 2,000 highly variable genes exhibiting the highest variance. The FindClusters function in Seurat was utilized to identify major cell subpopulations, using the default resolution setting (res = 1). Marker genes for various cell subpopulations were identified with Seurat. Cells were annotated by combining known lineage-specific marker genes with the online resource CellMarker (http://xteam.xbio.top/CellMarker/). Hierarchical clustering was then performed based on the enrichment activities of 28 immune-related signature to identify immune-related subtypes. Multiple TME decoding methodologies were employed to determine the composition of the TIME, including: ESTIMATE[35], CIBERSORT[36], quanTIseq[37], TIMER[38], and MCPcounter[39]. These analyses were performed using the R package IOBR[40], which facilitated the comprehensive exploration of the TIME and immune-related subtypes within the context of LOX + iCAF-related signature expression.

Differentially expressed genes identification and visualization

The limma package in the R software was employed to identify Differentially expressed genes (DEGs)[41]. DEGs between HNSCC samples in CAFs were selected based on the criteria |logFC|> 1 and P.adjust 0.85 and P.adjust < 0.05. The R package pheatmap was utilized to generate heatmaps and vlnplots to visualize the expression patterns of the identified DEGs.

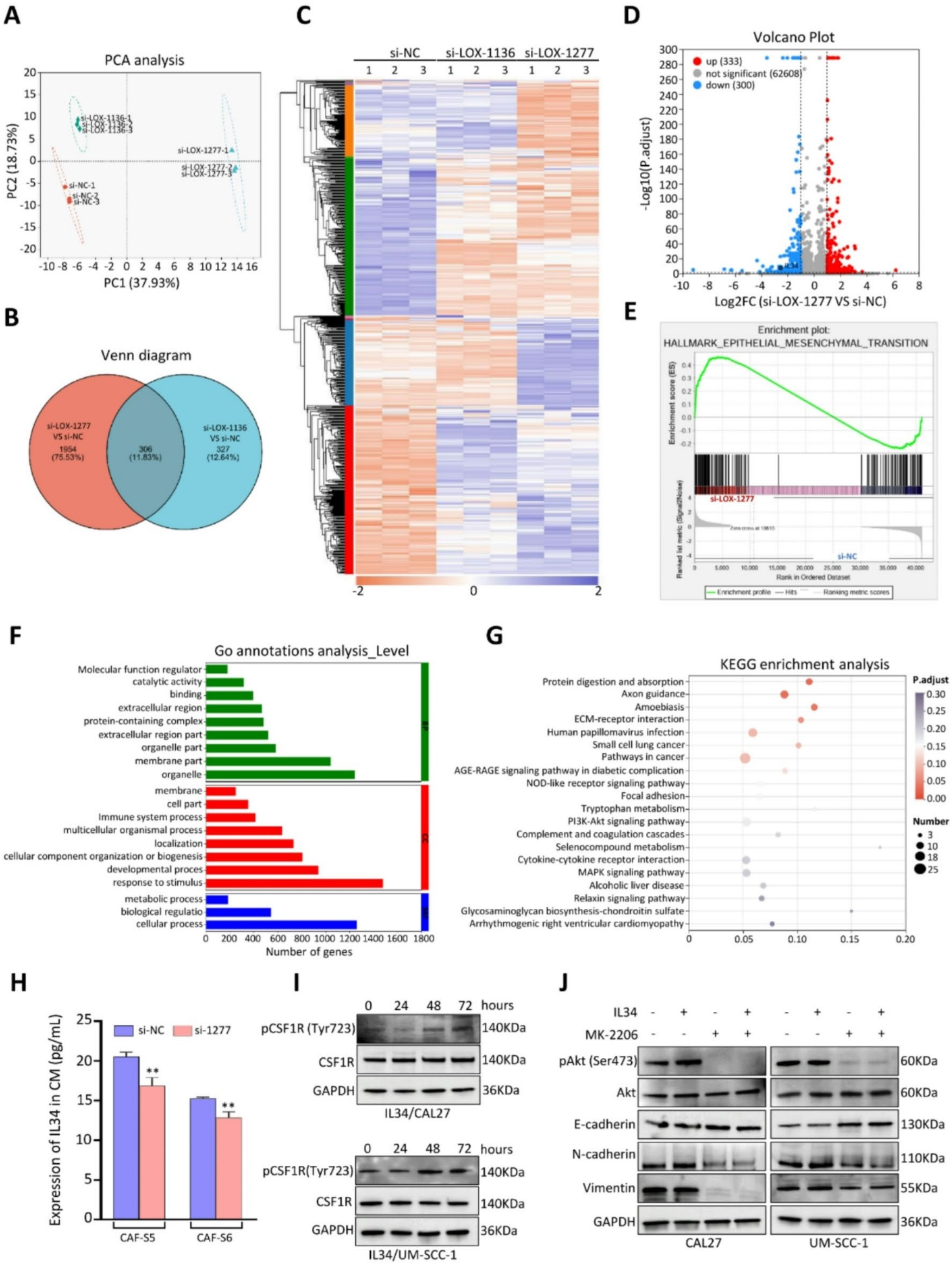

Enrichment analysis

In this project, Gene ontology (GO) and Kyoto encyclopedia of genes and genomes (KEGG) enrichment analysis was conducted using the clusterProfiler package. GO analysis categorized DEGs into three major categories: Biological Process, Cellular Component, and Molecular Function. The org.Hs.eg.db package was used as the annotation database for mapping the DEGs to the corresponding GO terms. The KEGG pathways enriched with the DEGs were identified and visualized to understand the molecular mechanisms underlying HNSCC. The outcomes of GO and KEGG enrichment analyses were visualized using the enrichplot and ggplot2 packages. A bubble plot was generated to depict the results of KEGG enrichment analysis, where each bubble represents a KEGG pathway, with the size of the bubble indicating the number of DEGs involved in the pathway and the color representing the significance level[42]. Gene set enrichment analysis (GSEA).

was performed to evaluate the biological features between molecular subtypes.

◀**Fig. 8**. IL34 activated CSF1R/Akt signaling pathway promoting EMT of OSCC. (A) PCA analysis of CAFs induced by transfection with NC, si-LOX-1136 and si-LOX-1277 in three repeated times. (B) Venn-diagram of DEGs between si-LOX-1136 vs. si-NC and si-LOX-1277 vs. si-NC. (C, D) Heatmap of confirmed the top DEGs of each group (C). Volcano plot illustrates the disparities in IL34 expression between the si-LOX-1277 and si-NC group (D). (E) GSEA analysis showed upregulated cancer hallmarks in CAFs induced by transfection with si-LOX-1277 (Left) compared with si-NC (Right). (F) Enriched GO enrichment analysis conducted to explore the relationship between the representative DEGs and their enriched pathways. (G) The bubble plot depict the results of the KEGG pathway analysis for DEGs (top 20 KEGG pathways of DEGs). (H) ELISA demonstrated the IL34 expression in the cultured supernatant of CAF-S5/-S6 induced by transfection with si-LOX-1277 and si-NC. (I) The level of pCSF1R(Tyr723), CSF1R in CAL-27 and UM-SCC-1 treatment with IL34 (100 ng/mL) in 0, 24, 48, 72 h examined by western blot ($n = 3$ per group). (J) The level of pAkt (Ser473), Akt, E-cadherin, N-cadherin, vimentin in CAL-27 and UM-SCC-1 treatment with or without MK-2206 inhibitor ($n = 3$ per group). For blots source data, see Fig. S4. ** $P < 0.01$;

H&E staining

4 μm-thick paraffin-embedded tumor tissues sections from 4 patients with HNSCC, who underwant surgical resection, were analyzed. The clinical and histopathological features of these HNSCC cases were documented and presented in Table S1. The sections were dewaxed using xylene to remove the paraffin and stained with hematoxylin (#H8070, Solarbio, Beijing, China) to visualize the nuclei. After staining with hematoxylin, the sections were washed with distilled water to remove excess stain. The sections were then stained with eosin (#G1100, Solarbio), which stains the cytoplasm and other tissue components. The stained sections were dehydrated using a series of graded ethanol solutions, followed by immersion in xylene. The air-dried sections were observed under an optical microscope (Leica DMi8, Wetzlar, Germany) to examine the histopathological features of the HNSCC tissues.

Immunofluorescence staining

Immunofluorescence staining was performed to detect the expression of specific proteins in tissues with preserved structure and organization. Slides were deparaffinized in BioClear New (Biognost, Shanghai, China) for 20 min each and then rehydrated by sequential incubation with 100%, 95%, 80%, and 75% ethanol, for 5 min each. Antigen retrieval was performed by incubating the slides in pH 6.0 citrate buffer (Solarbio) at 95 °C for 5 min. This step is critical for exposing the epitopes of the proteins of interest. Nonspecific binding sites were blocked with 10% QuickBlock Blocking Buffer (Beyotime Biotechnology, Shanghai, China). Slides were incubated with primary antibodies against FBLN1 (1:100; 20425-1-AP, Proteintech, Wuhan, China), CXCL12 (1:100; 17402-1-AP, Proteintech) overnight at 4 °C. Following day, the slides were washed with 1×TBST solution for 30 min to remove any unbound primary antibodies and slides were incubated with Goat Anti-Rabbit IgG H&L-AF488 (1:200; ab150077, Abcam, Cambridgeshire, UK) or Goat Anti-mouse IgG H&L-AF594 (1:200; ab150116, Abcam) as secondary antibodies for 60 min. Nuclei were counterstained with DAPI (1:3000, ThermoFisher Scientific, Waltham, MA, USA). The stained slides were observed under an inverted microscope (Leica DMi8), and images were recorded for analysis.

Ethics declarations

The study was approved by the Ethics Committee of Shanghai Stomatological Hospital, Fudan University (No.2024-023).

Cell culture

Primary CAFs were isolated from the fresh OSCC tissues using previously established methods[43] and designated as CAF-S5 and CAF-S6. Normal fibroblasts (NFs) were isolated from the normal gingival tissues of a healthy adult. CAFs and NFs were cultured in DMEM/F12 medium (Gibco, Grand Island, NY, USA) supplemented with 10% Fetal bovine serum (FBS, ScienCell, Carlsbad, CA, USA). CAL-27 was purchased from CELLCOOK and cultured in DMEM/High Glucose medium (Hyclone, Logan, UT, USA) supplemented with 10% FBS (ScienCell). UM-SCC-1 and U-937 was purchased from CELLCOOK and grown in DMEM 1640 medium (Hyclone) supplemented with 10% FBS (ScienCell). The culture medium for all cells were supplemented with 100U/mL penicillin and 100U/mL streptomycin (Hyclone) and maintained at 37 °C in a humidified atmosphere with 5% CO_2.

SiRNA transfection

Two LOX gene-specific short interfering RNAs (si-LOX-1136: 5′ - GCA CAG UUG UCA UCA ACA UTT – 3′ and si-LOX-1277: 5′- CAG GCG AUU UGC AUG UAC UTT – 3′) and a negative control siRNA (si-NC: 5′-UUC UCC GAA CGU GUC ACG UTT-3′) were synthesized by Genepharma (Shanghai, China). The synthesized siRNAs were transfected into CAFs using Lipofectamine™ 2000 reagent (ThermoFisher Scientific) according to manufacturer's instructions. After 72 h post-transfection, the total protein was isolated from the transfected CAFs. These proteins were then prepared for downstream applications such as western blot analysis to assess the efficiency of LOX silencing and its effects on the CAFs.

Preparation of conditioned medium

Conditioned medium (CM) from CAFs transfection with short interfering RNA was obtained as previously described[7]. In brief, CM was collected from CAFs transfected with si-NC, si-LOX-1136 and si-LOX-1277 was collected and then subjected to centrifugated at 500 ×g for 10 min, 2500 ×g for 20 min to remove any dead cells and cell debris, respectively. Then the supernatant was stored at -80 °C for use in subsequent experiments.

Cell treatment

U-937 cells were seeded at a density of 5×10^5 cells per well in a 12-well plate. Cells were treated with phorbol 12-myristate 13-acetate (PMA, 100 ng/mL, P8139, Sigma) for 48 h to induce differentiation into macrophages and then cultured in DMEM 1640 medium (Hyclone) supplemented with 10% FBS (ScienCell). After 48 h of differentiation, CM derived from CAFs silenced with LOX was added to each well for 48 h. To confirm IL34 promotes EMT of tumor cells, CAL-27 and UM-SCC-1 cells were seeded at a density of 5×10^4 cells per well in 6-well plates. Cells were allowed to adhere for 24 h under standard culture conditions. Following adhesion, cells were either unstimulated or stimulated with 100 ng/mL Recombinant human IL34 (#HY-P700125AF, MedChemExpress, Shanghai, China) for different time intervals of 0, 24, 48, and 72 h. To investigate the role of the Akt signaling pathway, 10 μM MK-2206 inhibitor (#HY-10358, MedChemExpress) was added to each well for 48 h during the IL34 stimulation. Cellular proteins were collected and then subjected to western blot analysis to assess the expression of markers associated with EMT and Akt signaling.

CCK8 assay

Cell viability assay using Cell Counting kit-8 (CCK8, CK04, Dojindo, Shanghai, China). CAL-27 and UM-SCC-1 cells were seeded in a 96-well plate at a density of 2×10^3 per well. Cells were allowed to adhere and cultured overnight under standard culture conditions. After overnight incubation, the cells were treated with CM derived from CAFs transfected with si-NC, si-LOX-1136, and si-LOX-1277 for 0, 24, 48, 72 h. 10 μL of CCK8 reagent was added to each well, which was mixed with 90 μL of DMEM/High medium and incubated for 1 h at 37℃. The absorbance at 450 nm was measured using a microplate reader (Bio-Rad, Hercules, CA, USA). Each treatment condition was performed in triplicate to ensure reliability. The mean absorbance values from the triplicate wells were calculated and used to assess cell proliferation rates.

Wound healing assay

CAL-27 and UM-SCC-1 cells were seeded into a six-well plate at a density of 4×10^5 cells per well. Cells were allowed to adhere and grow overnight. Next day, a wound was created in each well using a P1000 pipette tip to scratch the cell monolayer, simulating a wound in the cell layer. After creating the wound, the cells were treated with CM derived from CAFs transfected with si-NC, si-LOX-1136 and si-LOX-1277 and incubated for 48 h. The wound area was captured using an inverted microscope (Leica DMi8) at the start and end of the experiment to document the wound closure. Images were taken at multiple time points if necessary to monitor the migration process. Each condition was repeated in at least three wells to ensure statistical reliability.

Western blot

Cells were lysed with RIPA buffer (R0010, Solarbio) supplemented with protease inhibitor cocktail (HY-K0010, MedChemExpress) and phosphatase inhibitor cocktail I/II (HY-K0021, MedChemExpress) at 4℃ for 30 min. Protein concentration was determined by Pierce™ BCA Protein Assay Kits (23227, ThermoFisher Scientific). Equal volume and amount of proteins was separated by sodium dodecyl sulfate-polyacrylamide gel (SDS-PAGE). Proteins were transferred from the gel to a nitrocellulose membrane (Millipore Corporation, Billerica, MA, USA). The membrane was blocked with 5% fat-free milk for 2 h to prevent non-specific binding. The membrane was incubated with primary antibodies overnight at 4℃. Primary antibodies contained LOX (1:1000; ab174316, Abcam), FBLN1 (1:1000; 20425-1-AP, Proteintech), CD86 (1:1000; absin115477, Absin, Shanghai, China), iNOS (1:1000; abs155177, Absin), Phospho-CSF1R-Tyr723 (1:500; AP1075, Abclonal technology, Wuhan, China), CSF1R (1:500; #67455, Cell Signaling Technology, Danvers, MA, USA), Phospho-Akt-Ser473 (1:500; #4060, Cell Signaling Technology), Akt (1:1000; #9272, Cell Signaling Technology), E-cadherin (1:1000; ab314063, Abcam), N-cadherin (1:1000; ab76011, Abcam), vimentin (1:1000; 10366-1-AP, Proteintech), Fibroblast activation protein (FAP, 1:1000; #52818, Cell Signaling Technology), α-SMA (1:1000; ab7817, Abcam), GAPDH (1:5000; 10494-1-AP, Proteintech). After washing the membrane three times with 1×TBST and then incubated with Goat anti-Rabbit IgG (H + L) as secondary antibody (1:5000; #35401, Cell Signaling Technology) for 1 h. After the membrane washed three times with 1×TBST, and then protein bands were detected using an Enhanced chemiluminescence (ECL) detection system (ChemiDoc XRS, Bio-Rad).

ELISA

To reveal the content of IL34 in CM of CAFs transfection with si-LOX-1277 and si-NC, Human IL34 ELISA kit was purchased (JM-5955H2, Jingmei Biotechnology, Jiangsu, China). Standard solution was prepared for the serial dilution and CM from CAFs transfection with si-NC and si-1277 were added into each well (50 μL/well) and incubated at 37℃. After 30 min, HRP-Conjugate reagent was added into each well (50 μL) incubated at 37℃ for 30 min followed by incubation with Chromogen solution (100 μL) at 37℃ for 15 min. Add 50 μL of stop solution to each well to halt the reaction. Measure the absorbance at 450 nm using a microplate reader (ThermoFisher Scientific). Compare the absorbance values to the standard curve to determine the IL34 content in the CM samples.

RNA sequencing analysis

Total RNA was extracted from CAFs transfected with si-NC, si-LOX-1136 and si-LOX-1277 using TRIzol® Reagent (ThermoFisher Scientific) following the manufacturer's instructions. And then RNA quality was determined by 5300 Bioanalyser (Agilent) and quantified using the ND-2000 (NanoDrop Technologies). High-quality RNA sample was used to construct sequencing library. RNA purification, reverse transcription, library construction and sequencing were performed at Shanghai Majorbio Bio-pharm Biotechnology Co., Ltd. (Shanghai, China) according to the manufacturer's instructions (Illumina, San Diego, CA, USA). In brief, RNA sequencing was performed on an Illumina NovaSeq/HiSeq Xten using NovaSeq Reagent Kits. Raw paired end reads were trimmed and quality controlled by Fastp with default parameters. Reads were separately aligned to reference genome with orientation mode using HISAT2 software. The mapped reads of each sample were assembled byStringTie in a reference-based approach. To identify DEGs (differential expression genes) between different samples, the expression level of each transcript was calculated according to the transcripts per million (TPM) reads method. RSEM was used to quantify gene abundances. Essentially, differential expression analysis was performed using the DEGseq[44]. Functional-enrichment analysis including GO and KEGG were performed to identify which DEGs were significantly enriched in GO terms and metabolic pathways at Bonferroni-corrected p-value ≤ 0.05 compared with the whole-transcriptome background. GO functional enrichment and KEGG pathway analysis were carried out by Goatools and KOBAS[45], respectively.

Statistical analysis

R software (v 4.1.1) for statistical analyses. Shapiro–Wilk test and Levene's test was used for testing the normality and homogeneity properties, respectively. Visualize data distribution by plotting histograms using the histfunction in R. Assess using skewness() and kurtosis() functions from the moments R package. Categorical variables were compared through chi-squared test, and Wilcoxon rank-sum test or T test depending on the data distribution. Two-way analysis of variance (ANOVA) for comparing three or more groups. Determine relationships between variables using the Pearson correlation coefficient. Kaplan–Meier curves with the log-rank test were performed for survival analysis. GraphPad Prism 7.0 and Image J software for additional statistical analyses. A p-value of < 0.05 was regarded as significant results in statistics ($*p < 0.05$, $**p < 0.01$ and $***p < 0.001$). Unpaired Student's t-test was performed for comparisons between all of the data. Ensure all experiments are conducted at least three times and data are presented as mean ± SEM.

Data availability

The data sets analyzed for the current study are available from thecorresponding author on reasonable request. The authors declare that the data supporting the findings of this study are available within the paper and its Supplementary Information files. Should any raw data files be needed in another format they are available from the corresponding author upon reasonable request. The HNSCC scRNA-seq dataset was assessed via open-source data platform, GEO at https://www.ncbi.nlm.nih.gov/geo/query/acc.cgi? acc=GSE103322. The analysis can be assessed R software. The gene expression data of TCGA-HNSCC can be downloaded at https://portal.gdc.cancer.gov/projects/TCGA-HNSC. The dataset with HNSCC patients treated with PD-1/PD-L1 inhibitors along with clinical parameters was downloaded at https://www.ncbi.nlm.nih.gov/geo/query/acc.cgi. 26 stemness-related gene sets were obtained at stemchecker.sysbiolab.eu. The RNA sequencing data generated and analysed during the current study are available in the GSA-Human repository, https://ngdc.cncb.ac.cn/gsa-human.

Received: 15 October 2024; Accepted: 18 February 2025

References

1. Chen, C. et al. Crosstalk between cancer-associated fibroblasts and regulated cell death in tumors: insights into apoptosis, autophagy, ferroptosis, and pyroptosis. *Cell. Death Discov*. **1**, 189. https://doi.org/10.1038/s41420-024-01958-9 (2024).
2. Chen, Y., McAndrews, K. M. & Kalluri, R. Clinical and therapeutic relevance of cancer-associated fibroblasts. *Nat. Rev. Clin. Oncol.* **12**, 792–804. https://doi.org/10.1038/s41571-021-00546-5 (2021).
3. Mao, X. et al. Crosstalk between cancer-associated fibroblasts and immune cells in the tumor microenvironment: new findings and future perspectives. *Mol. Cancer*. **1**, 131. https://doi.org/10.1186/s12943-021-01428-1 (2021).
4. Rice, A. J. et al. Matrix stiffness induces epithelial-mesenchymal transition and promotes chemoresistance in pancreatic cancer cells. *Oncogenesis* **7**, e352. https://doi.org/10.1038/oncsis.2017.54 (2017).
5. Pei, L. et al. Roles of cancer-associated fibroblasts (CAFs) in anti- PD-1/PD-L1 immunotherapy for solid cancers. *Mol. Cancer*. **1**, 29. https://doi.org/10.1186/s12943-023-01731-z (2023).
6. Zhang, J. Y. et al. Cancer-associated fibroblasts promote oral squamous cell carcinoma progression through LOX-mediated matrix stiffness. *J. Transl Med.* **1**, 513. https://doi.org/10.1186/s12967-021-03181-x (2021).
7. Liu, X. et al. Carcinoma-associated fibroblast-derived Lysyl oxidase-rich extracellular vesicles mediate collagen crosslinking and promote epithelial-mesenchymal transition via p-FAK/p-paxillin/YAP signaling. *Int. J. Oral Sci.* **1**, 32. https://doi.org/10.1038/s41368-023-00236-1 (2023).
8. Gao, F. et al. Intra/Extracellular lactic acid exhaustion for synergistic metabolic therapy and immunotherapy of tumors. *Adv. Mater.* **51**, e1904639. https://doi.org/10.1002/adma.201904639 (2019).
9. Mei, H. et al. Carrier-free nanodrugs with efficient drug delivery and release for cancer therapy: from intrinsic physicochemical properties to external modification. *Bioact Mater.* **8**, 220–224. https://doi.org/10.1016/j.bioactmat.2021.06.035 (2021).
10. Chen, K. M., McAndrews, K. M. & Kalluri, R. Clinical and therapeutic relevance of cancer-associated fibroblasts. *Nat. Rev. Clin. Oncol.* **12**, 792–804. https://doi.org/10.1038/s41571-021-00546-5 (2021).
11. Öhlund, D. et al. Distinct populations of inflammatory fibroblasts and myofibroblasts in pancreatic cancer. *J. Exp. Med.* **3**, 579–596. https://doi.org/10.1084/jem.20162024 (2017).
12. Zhao, T., Li, T., Sun, L., Yuan, Y. & Zhu, Y. Potential mechanisms of cancer-associated fibroblasts in therapeutic resistance. *Biomed. Pharmacother*. **166**, 115425. https://doi.org/10.1016/j.biopha.2023.115425 (2023).
13. Ozga, A. J., Chow, M. T. & Luster, A. D. Chemokines and the immune response to cancer. *Immunity* **5**, 859–874. https://doi.org/10.1016/j.immuni.2021.01.012 (2021).
14. Hudson, W. H. et al. Proliferating transitory T cells with an Effector-like transcriptional signature emerge from PD-1^+ Stem-like $CD8^+$ T cells during chronic infection. *Immunity* **6**, 1043–1058e4 (2019).
15. Ma, C. et al. Pan-cancer spatially resolved single-cell analysis reveals the crosstalk between cancer-associated fibroblasts and tumor microenvironment. *Mol. Cancer*. **1**, 170. https://doi.org/10.1186/s12943-023-01876-x (2023).

16. Liang, T. et al. Cancer-Associated Fibroblast-Induced remodeling of tumor microenvironment in recurrent bladder Cancer. *Adv. Sci. (Weinh).* **31**, e2303230. https://doi.org/10.1002/advs.202303230 (2023).
17. Puram, S. V. et al. Single-Cell transcriptomic analysis of primary and metastatic tumor ecosystems in head and neck Cancer. *Cell* **7**, 1611–1624e24. https://doi.org/10.1016/j.cell.2017.10.044 (2017).
18. Zhang, Q. et al. Integrated analysis of single-cell RNA-seq and bulk RNA-seq reveals distinct cancer-associated fibroblasts in head and neck squamous cell carcinoma. *Ann. Transl Med.* **12**, 1017. https://doi.org/10.21037/atm-21-2767 (2021).
19. Jiang, Y., Li, Y. & Zhu, B. T-cell exhaustion in the tumor microenvironment. *Cell. Death Dis.* **6**, e1792. https://doi.org/10.1038/cddis.2015.162 (2015).
20. Huang, H. et al. Precursor exhausted CD8 + T cells in colorectal cancer tissues associated with patient's survival and immunotherapy responsiveness. *Front. Immunol.* **15**, 1362140. https://doi.org/10.3389/fimmu.2024.1362140 (2024).
21. Zhang, P. et al. IL-34 is a potential biomarker for the treatment of papillary thyroid cancer. *J. Clin. Lab. Anal.* **8**, e23335. https://doi.org/10.3389/fimmu.2024.1362140 (2020).
22. Wang, J. et al. The circEPSTI1/mir-942-5p/LTBP2 axis regulates the progression of OSCC in the background of OSF via EMT and the PI3K/Akt/mTOR pathway. *Cell. Death Dis.* **8**, 682. https://doi.org/10.1038/s41419-020-02851-w (2020).
23. Zhou, J. & Jin, S. Circ_0058063 contributed to oral squamous cell carcinoma development by sponging miR-145 and regulating PI3K/AKT pathway. *Mol. Biotechnol.* **12**, 2049–2060. https://doi.org/10.1007/s12033-023-00715-0 (2023).
24. Gunaydin, G. CAFs interacting with TAMs in tumor microenvironment to enhance tumorigenesis and immune evasion. *Front. Oncol.* **11**, 668349. https://doi.org/10.3389/fonc.2021.668349 (2021).
25. Chen, X. & Song, E. Turning foes to friends: targeting cancer-associated fibroblasts. *Nat. Rev. Drug Discov*. **2**, 99–115. https://doi.org/10.1038/s41573-018-0004-1 (2019).
26. Albinger–Hegyi, A. et al. Lysyl oxidase expression is an independent marker of prognosis and a predictor of lymph node metastasis in oral and oropharyngeal squamous cell carcinoma (OSCC). *Int. J. Cancer*. **11**, 2653–2662. https://doi.org/10.1002/ijc.24948 (2010).
27. Wuest, M. et al. Targeting Lysyl oxidase for molecular imaging in breast cancer. *Breast Cancer Res.* **7**, 107. https://doi.org/10.1186/s13058-015-0609-9 (2015).
28. Linares, J., Marín-Jiménez, J. A., Badia-Ramentol, J. & Calon, A. Determinants and functions of CAFs secretome during Cancer progression and therapy. *Front. Cell. Dev. Biol.* **8**, 621070. https://doi.org/10.3389/fcell.2020.621070 (2021).
29. Chen, Z. et al. Single-cell RNA sequencing highlights the role of inflammatory cancer-associated fibroblasts in bladder urothelial carcinoma. *Nat. Commun.* **1**, 5077. https://doi.org/10.1038/s41467-020-18916-5 (2020).
30. Hao, Y. et al. Integrated analysis of multimodal single-cell data. *Cell* **13**, 3573–3587e29. https://doi.org/10.1016/j.cell.2021.04.048 (2021).
31. Pinto, J. P. et al. StemChecker: a web-based tool to discover and explore stemness signatures in gene sets. *Nucleic Acids Res.* **W1**, W72–77. https://doi.org/10.1093/nar/gkv529 (2015).
32. Zhang, Z. et al. Pan-cancer landscape of T-cell exhaustion heterogeneity within the tumor microenvironment revealed a progressive roadmap of hierarchical dysfunction associated with prognosis and therapeutic efficacy. *EBioMedicine* **83**, 104207. https://doi.org/10.1016/j.ebiom.2022.104207 (2022).
33. Wang, Z. et al. Machine learning revealed stemness features and a novel stemness-based classification with appealing implications in discriminating the prognosis, immunotherapy and Temozolomide responses of 906 glioblastoma patients. *Brief. Bioinform.* **5**, bbab032. https://doi.org/10.1093/bib/bbab032 (2021).
34. Wilkerson, M. D. & Hayes, D. N. ConsensusClusterPlus: a class discovery tool with confidence assessments and item tracking. *Bioinformatics* **12**, 1572–1573. https://doi.org/10.1093/bioinformatics/btq170 (2010).
35. Yoshihara, K. et al. Inferring tumour purity and stromal and immune cell admixture from expression data. *Nat. Commun.* **4**, 2612. https://doi.org/10.1038/ncomms3612 (2013).
36. Chen, B. et al. Profiling tumor infiltrating immune cells with CIBERSORT. *Methods Mol. Biol.* **1711**, 243–259. https://doi.org/10.1007/978-1-4939-7493-1_12 (2018).
37. Finotello, F. et al. Molecular and Pharmacological modulators of the tumor immune contexture revealed by Deconvolution of RNA-seq data. *Genome Med.* **1**, 34. https://doi.org/10.1186/s13073-019-0638-6 (2019).
38. Li, T. et al. TIMER2.0 for analysis of tumor-infiltrating immune cells. *Nucleic Acids Res.* **W1**, W509–W514. https://doi.org/10.1093/nar/gkaa407 (2020).
39. Becht, E. et al. Estimating the population abundance of tissue-infiltrating immune and stromal cell populations using gene expression. *Genome Biol.* **1**, 218. https://doi.org/10.1186/s13059-016-1070-5 (2016).
40. Zeng, D. et al. IOBR: Multi-Omics Immuno oncology biological research to Decode tumor microenvironment and signatures. *Front. Immunol.* **12**, 687975. https://doi.org/10.3389/fimmu.2021.687975 (2021).
41. Ritchie, M. E. et al. Limma powers differential expression analyses for RNA sequencing and microarray studies. *Nucleic Acids Res.* **7**, e47. https://doi.org/10.1093/nar/gkv007 (2015).
42. Dai, F. et al. Integrated bioinformatic analysis of DNA methylation and immune infiltration in endometrial cancer. *Biomed. Res. Int.* **2022** (5119411). https://doi.org/10.1155/2022/5119411 (2022).
43. Li, J. et al. Small extracellular vesicle-bound vascular endothelial growth factor secreted by carcinoma-associated fibroblasts promotes angiogenesis in a bevacizumab-resistant manner. *Cancer Lett.* **492**, 71–83. https://doi.org/10.1016/j.canlet.2020.08.030 (2020).
44. Wang, L. et al. DEGseq: an R package for identifying differentially expressed genes from RNA-seq data. *Bioinformatics* **1**, 136–138. https://doi.org/10.1093/bioinformatics/btp612 (2019).
45. Xie, C. et al. KOBAS 2.0: a web server for annotation and identification of enriched pathways and diseases. *Nucleic Acids Res.* **39**, W316–W322. https://doi.org/10.1093/nar/gkr483 (2011).

Author contributions

Tingjiao Liu, Yuehua Liu, Xue Liu. Designed this study, did the experiments. Huibing Li, Qian Zhang. Data Curation. Yanjin Wang. Provided clinical samples. Xue Liu, Tingjiao Liu. Wrote the original manuscript.

Funding

This study was supported by the National Natural Science Foundation of China (82103423 82073001), Scientific Research Foundation for the Introduction of Talent in Shanghai Stomatological Hospital (SSDC-2021-RC05) and General Program (SSH-2024-A07) in Shanghai Stomatological Hospital, Shanghai Natural Science Foundation (23ZR1454800), Shanghai "Science and Technology Innovation Action Plan" Laboratory Animal Research Project (24141900800), National Key Clinical Program on Orthodontics and Shanghai Top Priority Research Center Program (2023ZZ02009).

Declarations

Competing interests
The authors declare no competing interests.

Additional information
Supplementary Information The online version contains supplementary material available at https://doi.org/10.1038/s41598-025-91036-6.

Correspondence and requests for materials should be addressed to Y.L. or T.L.

Reprints and permissions information is available at www.nature.com/reprints.

Publisher's note Springer Nature remains neutral with regard to jurisdictional claims in published maps and institutional affiliations.

Open Access This article is licensed under a Creative Commons Attribution-NonCommercial-NoDerivatives 4.0 International License, which permits any non-commercial use, sharing, distribution and reproduction in any medium or format, as long as you give appropriate credit to the original author(s) and the source, provide a link to the Creative Commons licence, and indicate if you modified the licensed material. You do not have permission under this licence to share adapted material derived from this article or parts of it. The images or other third party material in this article are included in the article's Creative Commons licence, unless indicated otherwise in a credit line to the material. If material is not included in the article's Creative Commons licence and your intended use is not permitted by statutory regulation or exceeds the permitted use, you will need to obtain permission directly from the copyright holder. To view a copy of this licence, visit http://creativecommons.org/licenses/by-nc-nd/4.0/.

© The Author(s) 2025